AN-92-9-3

NUMERICAL PREDICTION OF HORIZONTAL NONISOTHERMAL 3-D JET IN ROOM BASED ON ALGEBRAIC SECOND-MOMENT CLOSURE MODEL

S. Murakami, D.Eng.
Member ASHRAE

S. Kato, D.Eng.
Member ASHRAE

Y. Kondo

ABSTRACT

The three-dimensional nonisothermal jet in a room is analyzed numerically by the algebraic second-moment closure model (ASM) (Hossain and Rodi 1982). The numerical results are compared with experimental results and with a simulation based on the k-ε *model. It is demonstrated that ASM reproduces the nonisothermal flow fields more precisely than the* k-ε *model does.*

INTRODUCTION: FLOW FIELD IN A ROOM

In a preceding paper (Murakami et al. 1991), the accuracy and reliability of numerical simulation for three-dimensional nonisothermal jets in a room based on the k-ε model were examined. It was concluded that the correspondence between simulation and experiment was good from the viewpoint of practical use. However, the degree of the discrepancy in the case of nonisothermal flow apparently increased in the case of isothermal flow simulation. It was then suggested that this discrepancy arose from shortcomings of the eddy viscosity model (EVM) for Reynolds stress and the eddy diffusivity model (EDM) for turbulent flux. A more elaborate turbulence model, such as the algebraic second-moment closure model (ASM), would be required to increase the accuracy (Kato et al. 1991). In this paper, the authors apply the ASM to the same flow field in which they confirmed the validity of the simulation based on the k-ε model, and the increased accuracy and reliability of the simulation based on ASM are demonstrated.

The flow field in a room with supply and exhaust openings is typically an elliptic one in which there exist such various secondary flows as recirculation. It is so complex that sometimes the direction of the main flow cannot be found easily. There are many difficulties in analyzing such flow fields by a numerical method. As the flow field in a room is highly three-dimensional, it is difficult to deal with it two-dimensionally. In a three-dimensional calculation, it is usually impossible to arrange sufficiently fine mesh near the wall, so we are ordinarily forced to adopt the technique of the wall function at the wall boundary. Furthermore, the predominant terms of the mean strain-rate tensor ($\partial U_i/\partial x_j$) and scalar gradient ($\partial \Theta/\partial x_j$) vary locally, and thereby the effect of the streamline curvature usually cannot be neglected. Considering these complex conditions, the nonisothermal flow field in a room was analyzed by ASM and the results were compared with those of experiments and of simulations by the k-ε model. The authors focused in particular on the anisotropic property of the flow field. The structural differences between the two turbulence models were then examined.

MODEL FLOW FIELD

The configuration of the room model is shown in Figure 1. It is exactly the same as the model previously analyzed by the k-ε model (Murakami et al. 1991). A cold jet is discharged from the center of the left-hand wall. The right-hand wall, with an exhaust opening at each corner, is heated. The dimensions of the model are shown in Figure 1. The Archimedes number of the supply jet is 0.016.

Outline of Numerical Method

The standard k-ε model and the commonly adapted form for ASM were used. The equations are shown in Table 1 (also see Notes 1, 2, and 3).

The contribution of the buoyancy effect to the transport equations of turbulent energy, k, and turbulent energy dissipation rate, ε, is taken into account as G_k, following the method proposed by Viollet (1986) (see Note 3).

In the formulation of ASM, the convection term C_{ij} and the diffusion term D_{ij}, which include the derivatives of the Reynolds stress $\overline{u_i u_j}$ and the turbulent heat flux $\overline{u_i \theta}$, are expressed in a simplified way as shown in Equations 1 and 2, following the method of Rodi (1976) and Gibson and Launder (1976). The details are described in Kato et al. (1991).

Shuzo Murakami is a professor and **Shinsuke Kato** is an associate professor at the Institute of Industrial Science, University of Tokyo, Japan. **Yasushi Kondo** is a research engineer with Nikken Sekkei Ltd., Tokyo, Japan.

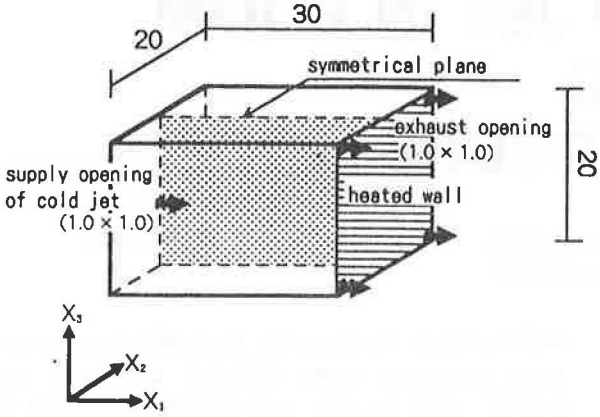

●Values are made dimensionless by
L_o (one side of supply or exhaust opening),
U_o (velocity at supply opening),
$\Delta\theta_o$ (temperature difference between exhaust and supply).
●In the experiment, U_o=1.0m/s, L_o=0.04m, $\Delta\theta_o$=12.2℃.
Cosequently at the supply opening,

Archimedes Number $A_r=\dfrac{-g_3\cdot\beta\cdot\Delta\theta_o\cdot L_o}{(U_o)^2}=0.016$,

and Reynolds number $R_e=2.7\times10^3$.
The scale of the room model
used for the experiment; 1.2m(x_1) × 0.8m(x_2) × 0.8m(x_3).
●In the numerical simulation, it is assumed that
$L_o=U_o=\Delta\theta_o=1.0$. Thus $A_r=-g_3\cdot\beta$ and
A_r is given the same value as in the experiment, 0.016.
g_3 is defined to be negative in this paper.

Figure 1 Room model used for simulation and experiment.

$$C_{ij}-D_{ij}=\frac{\overline{u_iu_j}}{k}(P_k+G_k-\varepsilon). \quad (1)$$

$$C_{i\theta}-D_{i\theta}=\frac{\overline{u_i\theta}}{2}\left(\frac{1}{k}(P_k+G_k-\varepsilon)+\frac{1}{\overline{\theta^2}}(P_\theta-\varepsilon_\theta)\right). \quad (2)$$

Table 2 shows the various numerical constants used in the model, which follow those proposed by Launder et al. (1975) and Launder (1983). The boundary conditions are shown in Table 3. Table 4 denotes grids and schemes for calculation.

A wall boundary condition of wall function is adopted, following Launder and Spalding (1974). At the heated wall on the right-hand side, the value of the heat flux is given as a boundary condition (Murakami et al. 1991).

Grid discretization is 35(x_1) × 22(x_2) × 54(x_3). Here x_1 denotes the horizontal direction of jet discharge and x_3 means the vertical direction. One-half of the space in the x_2 direction is analyzed, considering the symmetrical property of the flow field.

A staggered grid system is adopted. For the transport equations of U_i and scalar quantities (k and ε), a second-order upwind scheme (the QUICK scheme) is applied for

TABLE 1
Basic Equations of Algebraic Second-Moment Closure Model

(Continuity Eq.) $\dfrac{\partial U_i}{\partial x_i}=0$ (1)

(Momentum Eq.) $\dfrac{DU_i}{Dt}=-\dfrac{1}{\rho}\dfrac{\partial P}{\partial x_i}-\dfrac{\partial\overline{u_iu_j}}{\partial x_j}-g_i\beta\cdot\Theta$ (2)

(k-Eq.) $\dfrac{Dk}{Dt}=D_k+P_k+G_k-\varepsilon$ (3)

(ε-Eq.) $\dfrac{D\varepsilon}{Dt}=D_\varepsilon+\dfrac{\varepsilon}{k}(C_{\varepsilon1}P_k+C_{\varepsilon3}G_k-C_{\varepsilon2}\varepsilon)$ (4)

(Θ-Eq.) $\dfrac{D\Theta}{Dt}=\dfrac{\partial}{\partial x_j}(-\overline{u_j\theta})$ (5)

($\overline{\theta^2}$-Eq.) $\dfrac{D\overline{\theta^2}}{Dt}=D_\theta+P_\theta-\varepsilon_\theta$ (6)

($\overline{u_iu_j}$-Eq.) $(P_k+G_k-\varepsilon)\dfrac{\overline{u_iu_j}}{k}=P_{ij}+\Phi_{ij}+G_{ij}-\varepsilon_{ij}$ (7)

($\overline{u_i\theta}$-Eq.) $\dfrac{1}{2}\left(\dfrac{1}{k}(P_k+G_k-\varepsilon)+\dfrac{1}{\overline{\theta^2}}(P_\theta-\varepsilon_\theta)\right)\overline{u_i\theta}$

$=P_{i\theta(1)}+P_{i\theta(2)}+\Phi_{i\theta}+G_{i\theta}$ (8)

$D_k=\dfrac{\partial}{\partial x_m}(C_k\overline{u_mu_l}\cdot\dfrac{k}{\varepsilon}\cdot\dfrac{\partial k}{\partial x_l})$ (9) $D_\varepsilon=\dfrac{\partial}{\partial x_m}(C_\varepsilon\overline{u_mu_l}\cdot\dfrac{k}{\varepsilon}\cdot\dfrac{\partial\varepsilon}{\partial x_l})$ (10)

$D_\theta=\dfrac{\partial}{\partial x_m}(C_\theta\overline{u_mu_l}\cdot\dfrac{k}{\varepsilon}\cdot\dfrac{\partial\overline{\theta^2}}{\partial x_l})$ (11) $G_k=-\overline{u_i\theta}\cdot g_i\cdot\beta$ (12)

$P_k=-\overline{u_iu_j}\dfrac{\partial U_i}{\partial x_j}$ (13) $P_{ij}=-\overline{u_iu_k}\dfrac{\partial U_j}{\partial x_k}-\overline{u_ju_k}\dfrac{\partial U_i}{\partial x_k}$ (14)

$P_\theta=-2\cdot\overline{u_i\theta}\dfrac{\partial\theta}{\partial x_i}$ (15) $\varepsilon_{ij}=\dfrac{2}{3}\cdot\delta_{ij}\varepsilon$ (16)

$G_{ij}=-\overline{u_i\theta}\cdot g_j\cdot\beta-\overline{u_j\theta}\cdot g_i\cdot\beta$ (17) $G_{i\theta}=-g_i\cdot\beta\cdot\overline{\theta^2}$ (18)

$P_{i\theta(1)}=-\overline{u_ku_i}\dfrac{\partial\theta}{\partial x_k}$ (19) $P_{i\theta(2)}=-\overline{u_k\theta}\dfrac{\partial U_i}{\partial x_k}$ (20)

$\Phi_{ij}=\Phi_{ij(1)}+\Phi_{ij(2)}+\Phi_{ij(3)}+\Phi^w_{ij(1)}+\Phi^w_{ij(2)}$ (21) $\Phi_{ij(1)}=-C_1\dfrac{\varepsilon}{k}(\overline{u_iu_j}-\dfrac{2}{3}\delta_{ij}k)$ (22)

$\Phi_{ij(2)}=-C_2(P_{ij}-\dfrac{2}{3}\delta_{ij}P_k)$ (23) $\Phi_{ij(3)}=-C_3(G_{ij}-\dfrac{2}{3}\delta_{ij}G_k)$ (24)

$\Phi^w_{ij(1)}=\sum_{w=1}^{w_0}C'_1\dfrac{\varepsilon}{k}(\overline{u_ku_m}\cdot n_k^{(w)}\cdot n_m^{(w)}\cdot\delta_{ij}-\dfrac{3}{2}\overline{u_ku_i}\cdot n_k^{(w)}\cdot n_j^{(w)}-\dfrac{3}{2}\overline{u_ku_j}\cdot n_k^{(w)}\cdot n_i^{(w)})\cdot\dfrac{k^{3/2}}{C_l\cdot h_o^{(w)}\varepsilon}$ (25)

$\Phi^w_{ij(2)}=\sum_{w=1}^{w_0}C'_2(\Phi_{km(2)}\cdot n_k^{(w)}\cdot n_m^{(w)}\cdot\delta_{ij}-\dfrac{3}{2}\Phi_{ik(2)}\cdot n_k^{(w)}\cdot n_j^{(w)}-\dfrac{3}{2}\Phi_{kj(2)}\cdot n_k^{(w)}\cdot n_i^{(w)})\cdot\dfrac{k^{3/2}}{C_l\cdot h_o^{(w)}\varepsilon}$ (26)

$\Phi_{i\theta}=\Phi_{i\theta(1)}+\Phi_{i\theta(2)}+\Phi_{i\theta(3)}+\Phi^w_{i\theta(1)}$ (27) $\Phi_{i\theta(1)}=-C_{1\theta}\dfrac{\varepsilon}{k}\cdot\overline{u_i\theta}$ (28)

$\Phi_{i\theta(2)}=-C_{1\theta2}P_{i\theta(2)}$ (29) $\Phi_{i\theta(3)}=-C_{1\theta3}G_{i\theta}$ (30)

$\Phi^w_{i\theta(1)}=\sum_{w=1}^{w_0}C'_{1\theta1}\dfrac{\varepsilon}{k}\cdot\overline{u_k\theta}\cdot n_k^{(w)}\cdot n_i^{(w)}\cdot\dfrac{k^{3/2}}{C_l\cdot h_o^{(w)}\varepsilon}$ (31)

TABLE 2
Numerical Constants in Second-Moment Closure Model

C_1 :1.8	C_2 :0.6	C_3 :0.6	C'_1 :0.5	C'_2 :0.3	C_k :0.22	C_ε :0.16	$C_{\varepsilon 1}$:1.44	$C_{\varepsilon 2}$:1.92
$C_{\varepsilon 3}$:1.44(when $G_k>0$)	0.0(when $G_k\leq 0$)			C_θ :0.15	C_{w1} :3.0	C_{w2} :0.5	C_{w3} :0.3	C'_{w1} :0.5
C_r :2.5	σ_k : 1.0	σ_ε : 1.3	σ_θ : 1.0					

Nomenclature

U_i = average velocity component in i direction
u_i = fluctuating velocity component in i direction
U_o = velocity at supply opening
L_o = length of one side of supply or exhaust opening
$-\overline{u_iu_j}$ = Reynolds stress component
P = average pressure
k = turbulent kinetic energy
C_k = convection term of k
D_k = diffusion term of k
P_k = generation rate of k due to mean velocity gradient
G_k = generation term of k due to buoyancy effect
ε = dissipation rate of k
Θ = average value of scalar
θ = fluctuation of scalar
$\Delta\Theta_o$ = temperature difference between exhaust and supply
g_i = gravitational acceleration in i direction
β = coefficient of volumetric expansion ($\fallingdotseq$ 1/300)
$\overline{\theta^2}$ = mean square of scalar fluctuation
C_θ = convection term of $\overline{\theta^2}$
D_θ = diffusion term of $\overline{\theta^2}$
P_θ = generation rate of $\overline{\theta^2}$
ε_θ = dissipation rate of $\overline{\theta^2}$
C_{ij} = convection term of $\overline{u_iu_j}$
D_{ij} = diffusion term of $\overline{u_iu_j}$
P_{ij} = generation rate of $\overline{u_iu_j}$ due to velocity gradient
G_{ij} = generation rate of $\overline{u_iu_j}$ due to buoyancy effect
ε_{ij} = dissipation rate of $\overline{u_iu_j}$
Φ_{ij} = pressure-strain correlation term (consists of Rotta term $\Phi_{ij(1)}$, rapid term $\Phi_{ij(2)}$, $\Phi_{ij(3)}$ and wall reflection term $\Phi^w_{ij(1)}$, $\Phi^w_{ij(2)}$)
$C_{i\theta}$ = convection term of $\overline{u_i\theta}$
$D_{i\theta}$ = diffusion term of $\overline{u_i\theta}$
$P_{i\theta}$ = $P_{i\theta(1)}+P_{i\theta(2)}$ =generation rate of $\overline{u_i\theta}$ by mean temperature and velocity gradient ,respectively
$G_{i\theta}$ = generation rate of $\overline{u_i\theta}$ due to temperature fluctuation $\overline{\theta^2}$
$\Phi_{i\theta}$ = correlation term of pressure and scalar gradient
A_r = Archimedes number ($\equiv -g_3\cdot\beta\cdot\Delta\Theta_o\cdot L_o/(U_o)^2$)
R_e = Reynolds number at supply opening($\equiv U_o\cdot L_o/\nu$)
σ_k = turbulent Prandtl number for k
σ_ε = turbulent Prandtl number for ε
σ_θ = turbulent Prandtl number for Θ
$h_n^{(w)}$ = vertical distance from the w-th wall
δ_{ij} = kronecker delta

Superscripts

" $\overline{\ }$ " = averaging operation
"wo" = total number of boundaries which enclose each region
"(w)" = the w-th wall

Subscripts

i, j, k= spatial coordinate indices
1: streamwise direction(jet discharging direction)
2: lateral direction
3: vertical direction.

Values are made dimensionless by L_o, U_o and $\Delta\Theta_o$.

TABLE 3
Boundary Conditions (Expressed by Dimensionless Value)

(Boundary at supply opening) $U_{IN}=1.0$ $k_{IN}=0.0018$ $\ell_{IN}=0.325$ $\Theta_{IN}=0.0$ $\overline{u_au_i}=0$

(Boundary at exhaust opening) $U_{OUT}=0.25$ k,ε,Θ : free slip condition $\overline{u_au_i}=0$

(Wall boundary) The wall shear stress τ_w is given by equation ①, following Launder and Spalding(1974). Velocity gradient at the wall is given by equation ②, which is used to calculate the generation term at the near-wall node. The value of ε at the near-wall node used for the transport equation for k is expressed by equation ③,as a form averaged in a control-volume, and defined as $\bar{\varepsilon}$. The value of k at the wall is given by free slip condition. The value of ε at the near-wall node used for the transport equation of ε is defined by equation ④.

$$\frac{U_1}{(\tau_w/\rho)}(C_\mu^{1/2}k)^{1/2}=\frac{1}{\kappa}\ell_n\left[\frac{E(h_1/2)\cdot(C_\mu^{1/2}k)^{1/2}}{\nu}\right] \quad ①, \qquad \left\{(\nu+\nu_t)\cdot\frac{\partial U}{\partial y}\right\}\Big|_{WALL}=\tau_w/\rho \quad ②,$$

$$\varepsilon=\frac{C_\mu^{3/4}k^{3/2}}{\kappa(h_1/2)}\cdot\ell_n\left[\frac{E(h_1/2)\cdot(C_\mu^{1/2}k)^{1/2}}{\nu}\right] \quad ③, \qquad \varepsilon_1=\frac{C_\mu^{3/4}\cdot k^{3/2}}{\kappa(h_1/2)} \quad ④.$$

Heat flux at heated wall : $\overline{u_1\theta}=-0.0025$. Heat flux at other walls $\overline{u_n\theta}=0.0$.
$\kappa=0.4$, $C_\mu=0.09$, $E=9.0$, $\nu=1/R_e=1/(2.7\times10^3)$

TABLE 4
Grids and Schemes for Calculation

The computational domain is discretized into $35(x_1) \times 22(x_2) \times 54(x_3)$.

One side of the supply and exhaust openings is divided into 4 grids. Minimum grid size is 0.25 and maximum is 1.0.

One – half space of x_2 direction is calculated, considering the symmetrical property of the flowfield.

The convection term of U_i, k and ε is calculated by means of the QUICK scheme, except for the area just around the supply and exhaust openings, where the first-order upwind scheme is used. For the calculation of Θ, the first-order upwind scheme is used for the whole domain.

The generation of $\overline{u_i\theta}$ due to $\overline{\theta^2}$ was not considered, because this generation was estimated through preliminary analysis to be much smaller than the generation due to velocity gradient or temperature gradient. Consequently, calculations for $\overline{\theta^2}$ and ε_θ are not made. The local equilibrium for $\overline{\theta^2}$ is assumed for the calculation of Eq.(33).

the convection terms. The Adams-Bashforth scheme is used for time marching. The numerical integration is conducted following the ABMAC method (simultaneous iteration method for pressure and velocity).

Outline of Model Experiment

The scale of the model for the experiment is 1.2 m (x_1) × 0.8 m (x_2) × 0.8 m (x_3), as shown in Figure 1. The outside of the model is thermally insulated.

The accurate measurement of air velocity in a three-dimensional nonisothermal flow field is very difficult. A 3-D ultrasonic velocimeter of 5-cm span is utilized in this experiment, whose dependency on ambient air is only related to air density and can be compensated exactly. One shortcoming of this anemometer is the wideness of the averaging length (5 cm); thus the values of the mean velocity components U_i, turbulent energy k, Reynolds stress $\overline{u_iu_j}$, etc., are given as the average of 5 cm. Therefore, the measuring interval of the velocity is of necessity much larger than that of the temperature, as is shown in Figures 2 and 3.

Temperature is measured by copper-constantan thermocouples. The heat generation rate at the right-hand heating wall is measured by an electronic power meter.

RESULTS AND DISCUSSION

Distribution of Mean Velocity U_i

The distribution of the velocity vectors and resultant velocities ($\sqrt{U_1^2 + U_2^2 + U_3^2}$) at the central vertical section are illustrated in Figures 2 and 4.

The velocity values in the area around the center of the jet are very important. Except for the area just after the jet discharge, the velocity distributions predicted by ASM denote less steep gradients than those given by the standard k-ε model. ASM corresponds to the experiment better than the k-ε model does. This is attributed to the fact that the evaluation of the Reynolds stress $\overline{u_iu_j}$ in the momentum equation given by ASM is more accurate than that given by the k-ε model. A comparison of $\overline{u_iu_j}$ between ASM and the k-ε model is in Appendix A. The downward movement of the center of the cold jet due to the buoyancy effect given by ASM is a little smaller than that given by the k-ε model, since ASM predicts a smaller temperature difference in the area around the center of the jet, as shown in Figure 3.

Distribution of Mean Temperature Θ

The mean temperature distributions in the model are shown in Figures 3 and 5. The temperature distribution in the area around the center of the jet is also very important. Except for the area just after the jet discharge, the distributions given by ASM generally show less steep gradients than those given by the k-ε model. The results of ASM correspond to the experiment better than the k-ε model does, showing the same tendency as in the case of the velocity distribution. This is caused by the difference in the evaluation of the turbulent heat flux $\overline{u_i\theta}$ (Murakami kami et al. 1991). Since ASM predicts a larger value of $\overline{u_i\theta}$ than the k-ε model does (Figure 8), the diffusion of the temperature difference around the center of the jet in the case of ASM is more active than that given by the k-ε model.

The results of both ASM and the k-ε model show poor agreement with the experimental results for the area below and above the jet just after the discharge. Some comments concerning this poor agreement are given in Note 4.

Distribution of Turbulent Energy k

Figure 6 shows the distribution of turbulent kinetic energy k. In the area just after the discharging of the jet, where both ASM and the k-ε model show steep gradients of velocity and temperature, the predicted value of k given by ASM is larger than that given by the k-ε model. This is caused by the fact that ASM predicts the values of the

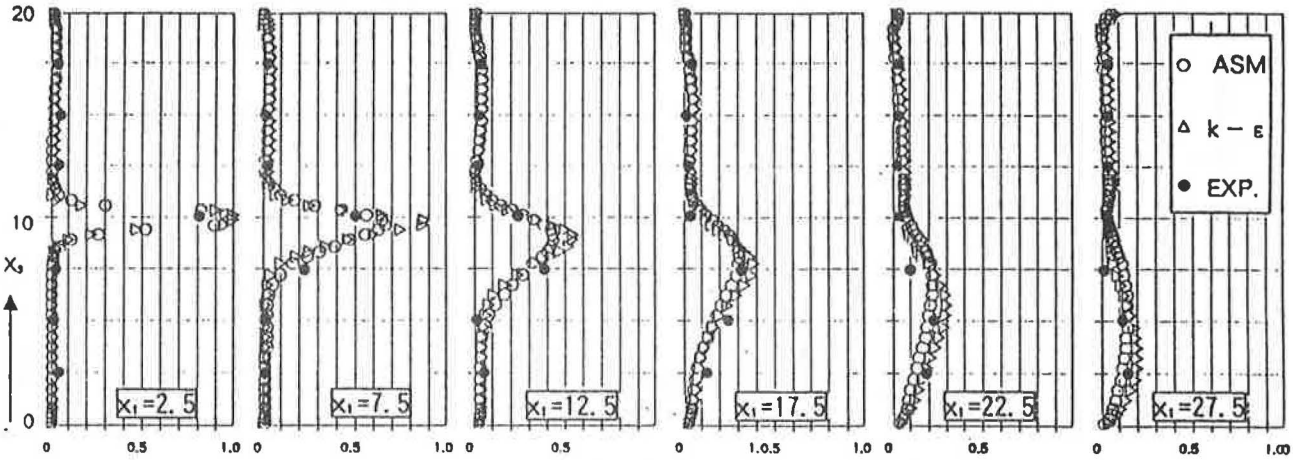

Figure 2 *Comparison of resultant velocity distribution* $U = \sqrt{U_1^2 + U_2^2 + U_3^2}$ *(dimensionless value by* U_o*, at center section).*

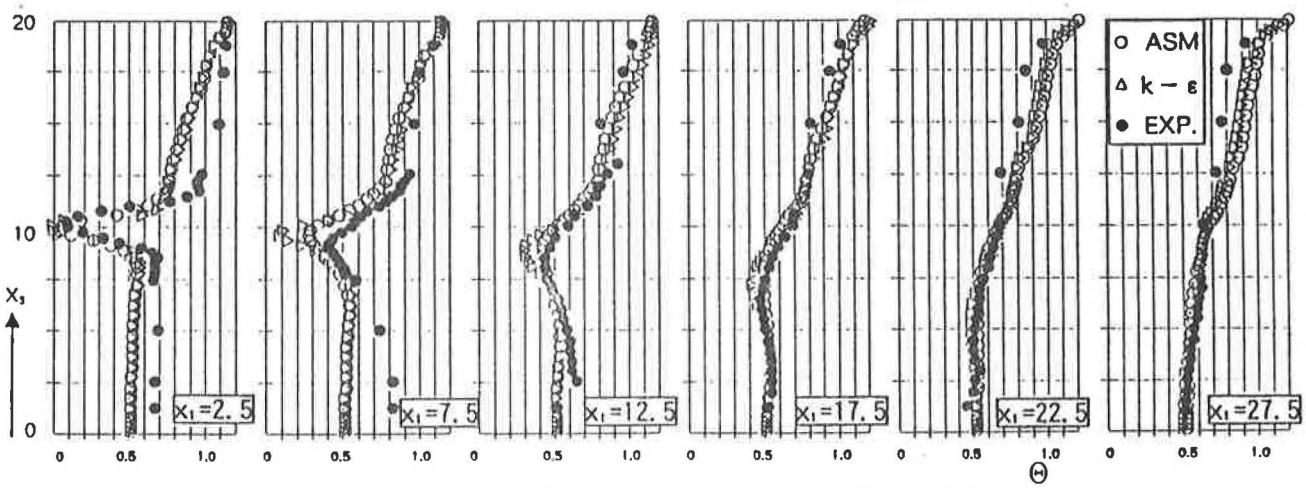

Figure 3 *Comparison of temperature distribution* Θ *(dimensionless value by* $\Delta\Theta_o$*, at center section).*

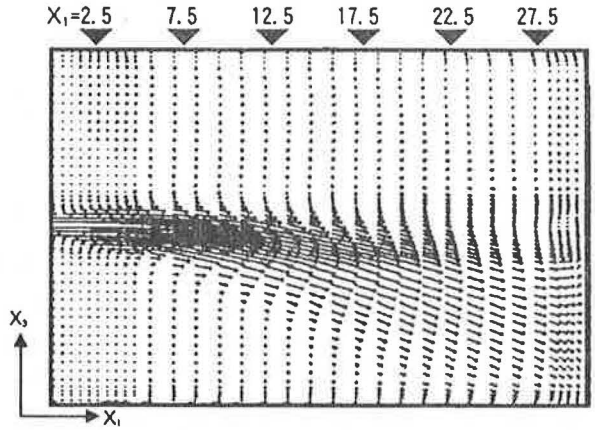

Figure 4 *Distribution of velocity vector (result of ASM at center section).*

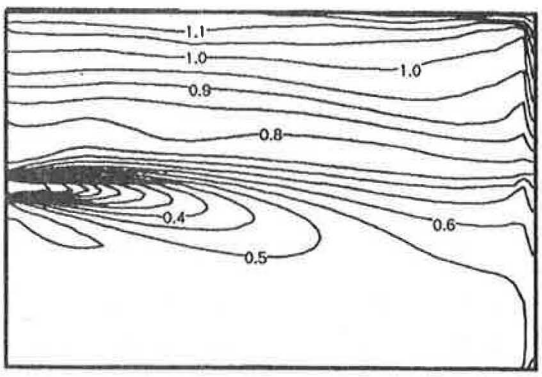

Figure 5 *Distribution of temperature* Θ *(result of ASM at center section).*

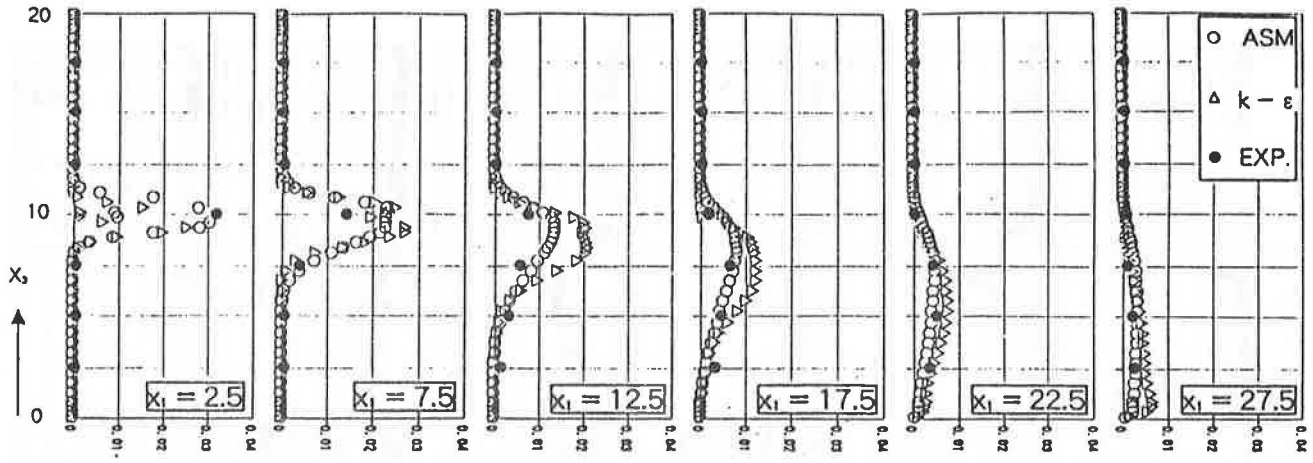

Figure 6 *Comparison of turbulence energy* k.

Reynolds stress ($\overline{u_i u_j}$) more accurately and accordingly predicts the value of kinetic energy generation by mean shear P_k more successfully than does the k-ε model. Except for the area near the supply opening, the value of k given by ASM is smaller than that given by the k-ε model because ASM denotes less steep gradients of velocity and temperature in these areas. The numerical results of ASM agree well with the experimental results.

Distribution of the Generation Term P_k of k Due to Mean Shear

Figure 7 shows the distribution of P_k. The value of P_k given by ASM is larger in the area near the supply opening than that given by the k-ε model because ASM evaluates the value of $\overline{u_i u_j}$ more accurately. The accurate evaluation of $\overline{u_i u_j}$ is particularly important in this flow field since the predominant velocity gradient in this area is $\partial U_1/\partial X_3$, as described in Appendix A.

Distribution of Heat Flux $\overline{u_i \theta}$

The distribution of turbulent heat flux $\overline{u_i \theta}$ is shown in Figure 8. The values of $\overline{u_i \theta}$ predicted by ASM and the k-ε model show large differences. In particular, the difference for streamwise heat flux $\overline{u_1 \theta}$ is remarkable. The value of $\overline{u_1 \theta}$ predicted by the k-ε model is much smaller than the result given by ASM. Since $\overline{u_1 \theta}$ is calculated by $-\nu_t/\sigma_\theta \cdot \partial\Theta/\partial x_1$ with the k-ε model and $\partial\Theta/\partial x_1$ is small in this flow field, the predicted value of $\overline{u_1 \theta}$ is also small. However, in the case of ASM, all terms of

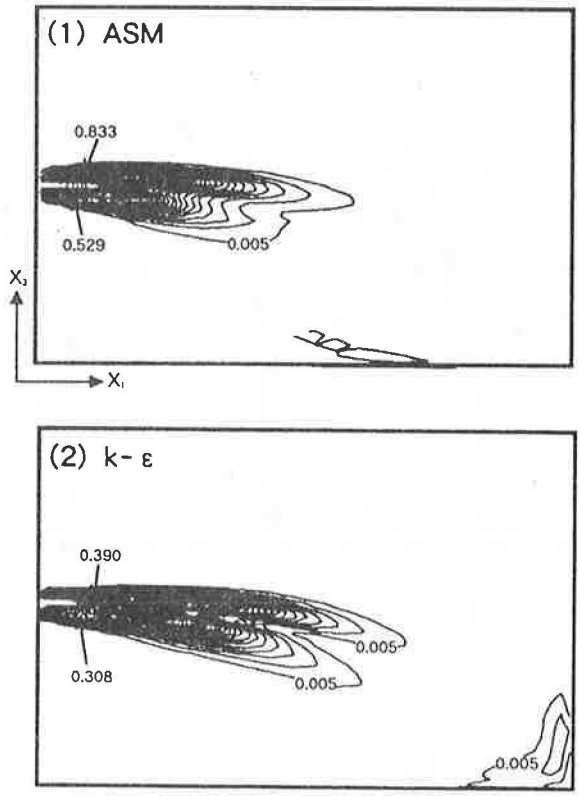

Figure 7 *Comparison of generation term of* k (P_k).

the generation by temperature gradient $P_{i\theta(1)}$ ($= -\overline{u_k u_i}\,\partial\Theta/\partial x_k$) and velocity gradient $P_{i\theta(2)}$ ($= -\overline{u_k \theta}\,\partial U_i/\partial x_k$) are evaluated exactly. Hence, the contribution of the predominant term of the temperature gradient $\partial\Theta/\partial x_3$ and the predominant term of the velocity gradient $\partial U_1/\partial x_3$ to the production of $\overline{u_1 \theta}$ is reflected correctly. Thus the value of $\overline{u_1 \theta}$ given by ASM becomes large. The structure

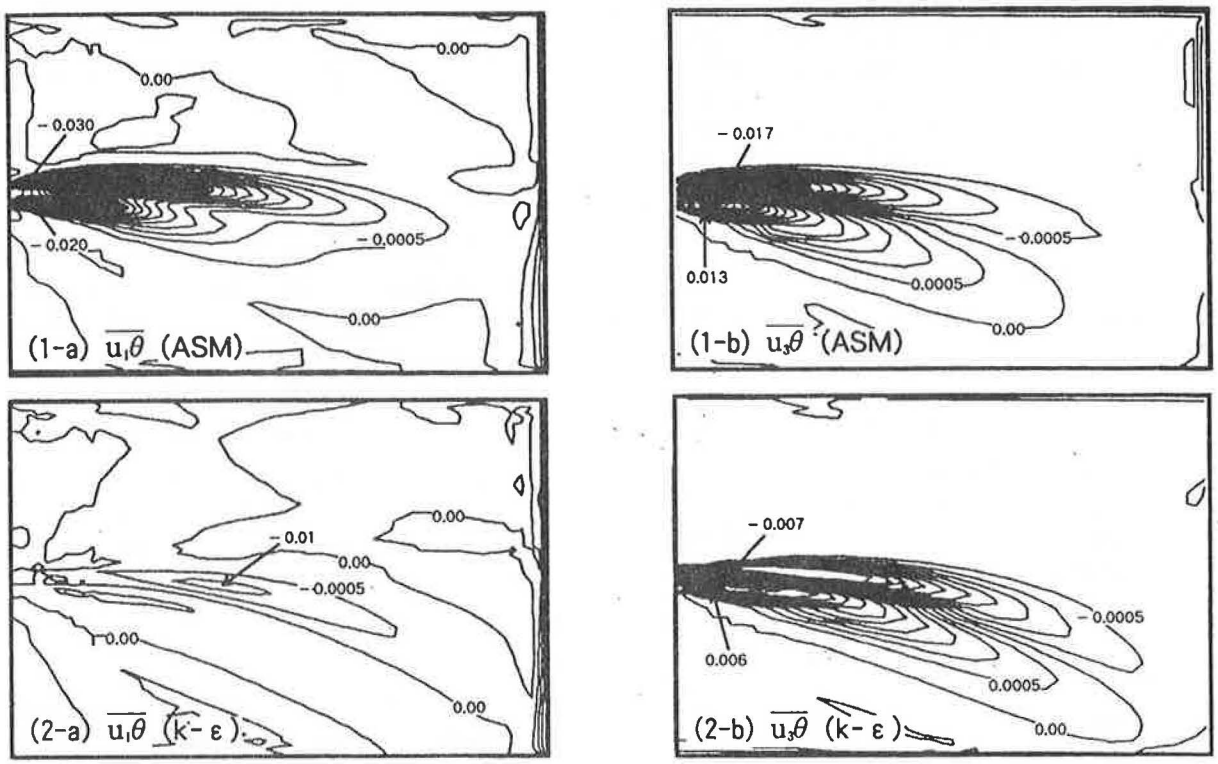

Figure 8 *Comparison of turbulent heat flux,* $\overline{u_i\theta}$.

causing the large production of $\overline{u_1\theta}$ in this flow field is illustrated in Figure 9.

This large value of $\overline{u_1\theta}$ is reflected in the temper- distribution; thus the distribution given by ASM becomes less steep and agrees with the experiment better than does the *k-ε* model.

CONCLUSION

The three-dimensional anisotropic flow field with buoyancy has been analyzed by ASM and the numerical results compared with experimental ones and with those given by the *k-ε* model.

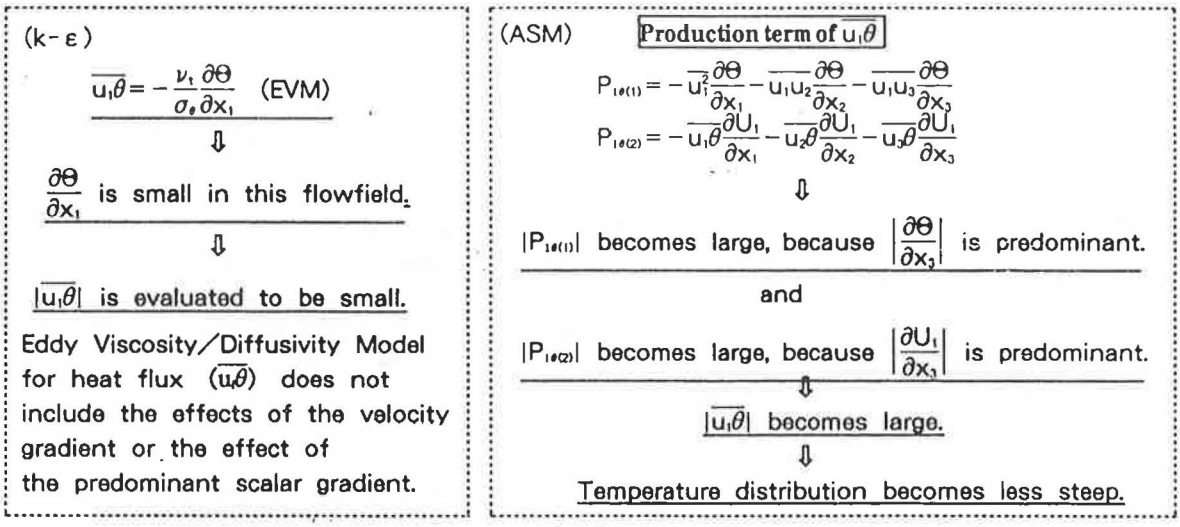

Figure 9 *Difference of evaluation of* $\overline{u_i\theta}$ *between* k-ε *model and ASM.*

1. The distributions of mean velocity U, mean temperature Θ, and turbulent kinetic energy k, predicted by ASM generally denote less steep gradients and correspond to the experiment better than results of the k-ε model. This advantage of ASM over the k-ε model is attributed mainly to the difference in the evaluation of Reynolds stress $\overline{u_i u_j}$ and turbulent heat flux $\overline{u_i \theta}$. These terms are calculated using the exact form in the case of ASM, whereas they are calculated on the basis of the eddy viscosity model by the k-ε model.
2. The anisotropic property of $\overline{u_i u_j}$ in the jet region is well reproduced by ASM, but the k-ε model reproduces this characteristic less exactly. This difference is attributed to the difference in the method of evaluating the generation term P_{ij}. Furthermore, the difference of $\overline{u_i \theta}$ predicted by ASM and the k-ε model, in particular the difference in $\overline{u_i \theta}$, is also remarkable. The result given by ASM is better.
3. It is clear that the k-ε model is less accurate than ASM for nonisothermal flow. Although the concept of a locally determined, isotropic, effective turbulent diffusivity is, of course, very useful, it may be concluded that such values as the turbulent flux of $\overline{u_i u_j}$, $\overline{u_i \theta}$, etc., in an anisotropic nonisothermal flow field cannot be predicted with full exactness by means of simple eddy viscosity modeling.
4. Second-moment closure modeling, even if only a simple version such as ASM, appears to be very effective for the analysis of complex flow fields.

Note 1

The equations in Table 1 are not expressed in dimensionless form. For example, the buoyancy term $(-g_i \cdot \beta \cdot \Theta)$ is expressed as $(\mathrm{Ar} \cdot \Theta')$ by nondimensionalization. Here Θ' is the dimensionless temperature.

Note 2

$\Phi^w_{ij(2)}$ is not involved in this calculation. This is because the Gibson-Launder (1978) model of $\Phi^w_{ij(2)}$, which is most common at present, appears to have some shortcomings in the analysis of an enclosed space with impinging (Kato et al. 1991). The reason is as follows.

Let us imagine a situation of impinging in which a mean flow (U_1) attacks the opposite wall $x_2 - x_3$ perpendicularly. In this situation, $\Phi^w_{ij(2)}$ may be represented in the following manner:

$$\Phi^w_{11(2)} = 2C_2C_2'(P_{11} - 2/3P_k) \cdot f_1,$$

$$\Phi^w_{22(2)} = \Phi^w_{33(2)} = -C_2C_2'(P_{11} - 2/3P_k) \cdot f_1.$$

Here

$$f_1 = k^{3/2}/(2.5 \cdot \varepsilon \cdot h_1).$$

$\Phi^w_{11(2)}$ is the term that should decrease $\overline{u_1^2}$ according to its original meaning. Thus, in this case, $(P_{11} - 2/3P_k)$ must be negative. However, on the centerline of the impinging jet, P_{11} is large. Therefore, it does not take a negative value. Hence, in this model, $\Phi^w_{11(2)}$ works to increase $\overline{u_1^2}$, contrary to its original meaning. As a matter of fact, when $\Phi^w_{ij(2)}$ is involved in the calculations, the normal stress perpendicular to the wall becomes excessively large near the exhaust opening and the solution diverges.

Note 3

The ε equation is so revised that an expression of buoyancy generation/destruction is switched according to the locally determined thermal instability, following the method proposed by Viollet (1986) as follows.

When $G_k > 0$, $C_3 = C_1 = 1.44$, and when $G_k \leq 0$, $C_3 = 0$.

Note 4

Since the jet is discharged into stagnant air, the air velocity is almost zero in the area above and below the jet just after discharging, as shown in Figures 2 and 4. The agreement for the temperature distribution between the experiment and the numerical simulation is poor in this area. The reason for the disagreement may be explained as follows:

1. Since the air velocity is very low in such an area, the slow secondary flows caused by the disturbance of the experimental condition become rather effective, which gives rise to uncertainty in the experimental results. The realization of a strictly controlled experimental condition is very difficult for such types of flow and temperature fields.
2. Although the turbulence models are based on the assumption that the flow field is fully turbulent, the Reynolds number in this area is rather low and not fully turbulent.
3. There is some possibility that the simulation has not yet reached a steady state.

REFERENCES

Gibson, M.M., and B.E. Launder. 1976. On the calculation of horizontal turbulent free shear flows under

gravitational influence. *J. Heat Transfer, Trans. ASME* (Feb.): 81-87.

Gibson, M.M., and B.E. Launder. 1978. Ground effects on pressure fluctuations in the atmospheric boundary layer. *J. Fluid Mech.* 86: 491.

Hossain, M.S., and W. Rodi. 1982. A turbulence model for buoyant flows and its application to vertical buoyant jets. In *Turbulent Buoyant Jets and Plumes*, W. Rodi, ed., HMT-Series, Vol. 6. Oxford, UK: Pergamon Press.

Kato, S., S. Murakami, and Y. Kondo. 1991. Numerical simulation of 2-D room airflow with and without buoyancy by means of ASM. Unpublished.

Launder, B.E. 1983. Second-moment closure, methodology and practice. Univ. Manchester Institute of Sci. and Tech., Rep. No. TFD/82/4.

Launder, B.E., and J.L. Spalding. 1974. The numerical computation of turbulent flow. *Computer Methods in Applied Mechanics and Engineering* 3: 269-289.

Launder, B.E., G.J. Reece, and W. Rodi. 1975. Progress in the development of a Reynolds-stress turbulence closure. *J. Fluid Mech.* 68: 537-566.

Murakami, S., S. Kato, and H. Nakagawa. 1991. Numerical prediction of horizontal nonisothermal 3-D jet in room based on the *k-ε* model. *ASHRAE Transactions* 97(1): 38-48.

Rodi, W. 1976. A new algebraic relation for calculating the Reynolds stresses. *ZAMM* (56): T219-T221.

Viollet, P.L. 1986. On the numerical modelling of the stratified flows. *Proc. Symposium Physical Processes in Estuarie.*

APPENDIX A

DISTRIBUTION OF REYNOLDS STRESS $\overline{u_i u_j}$

As shown in Figures A1, A2, A3, and A4, the values of each component of the Reynolds stress $\overline{u_i u_j}$ given by ASM agree very well with those given by the experiment. In particular, the anisotropic property of normal stress $\overline{u_i u_i}$ is reproduced very well. The value of $\overline{u_1^2}$ thus becomes two times larger than $\overline{u_2^2}$ and $\overline{u_3^2}$ in the case of ASM, as can be observed in the experiment, while the *k-ε* model fails to reproduce this anisotropic property. The comparison of $\overline{u_i u_j}$ between the experiment and the simulation is difficult in the area just after the supply opening because the average length of the anemometer is rather large (5 cm) and the values of $\overline{u_i u_j}$ are averaged within this length in the experiment, whereas the numerical results have very steep gradients with two peaks here.

Figure A6 illustrates the difference between ASM and the *k-ε* model in the evaluation of $\overline{u_i u_i}$. ASM evaluates each component of P_{ij} using its exact form. Since the velocity gradient of $\partial U_1/\partial x_3$ is predominant here and is included only in P_{11}, the value of P_{11} is much larger than P_{22} and P_{33}, as shown in Figure A5. Consequently, $\overline{u_1^2}$ becomes about two times larger than $\overline{u_2^2}$ and $\overline{u_3^2}$. However, in the *k-ε* model, a component of the normal stress is shown as below.

$$\overline{u_1^2} = -2 \cdot \nu_t (\partial U_i/\partial x_i) + 2/3 \cdot k$$

(no summation here).

Thus each component of $\overline{u_1^2}$ has similar values and becomes apparently isotropic.

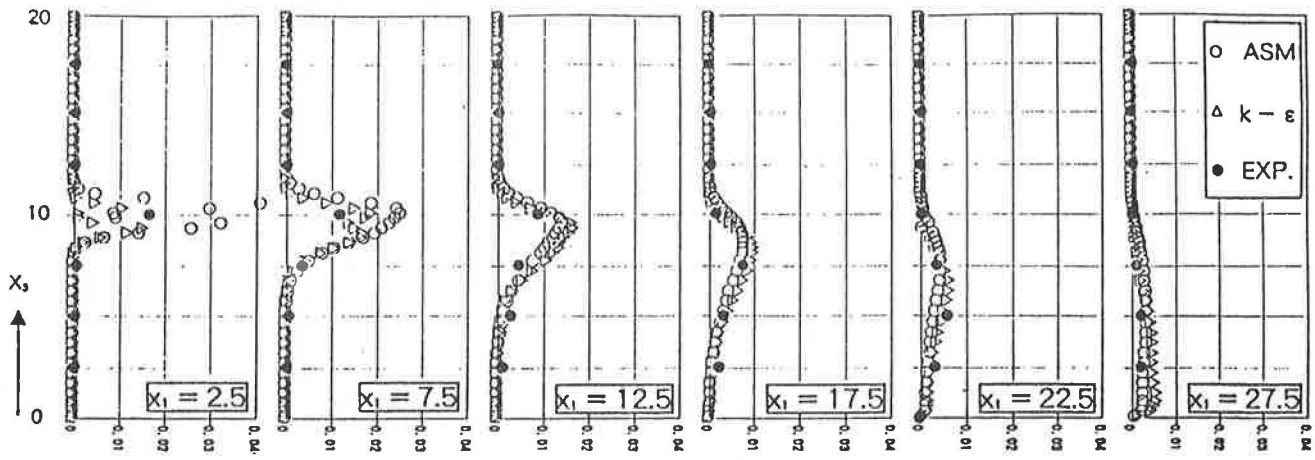

Figure A1 Distribution of $\overline{u_1^2}$.

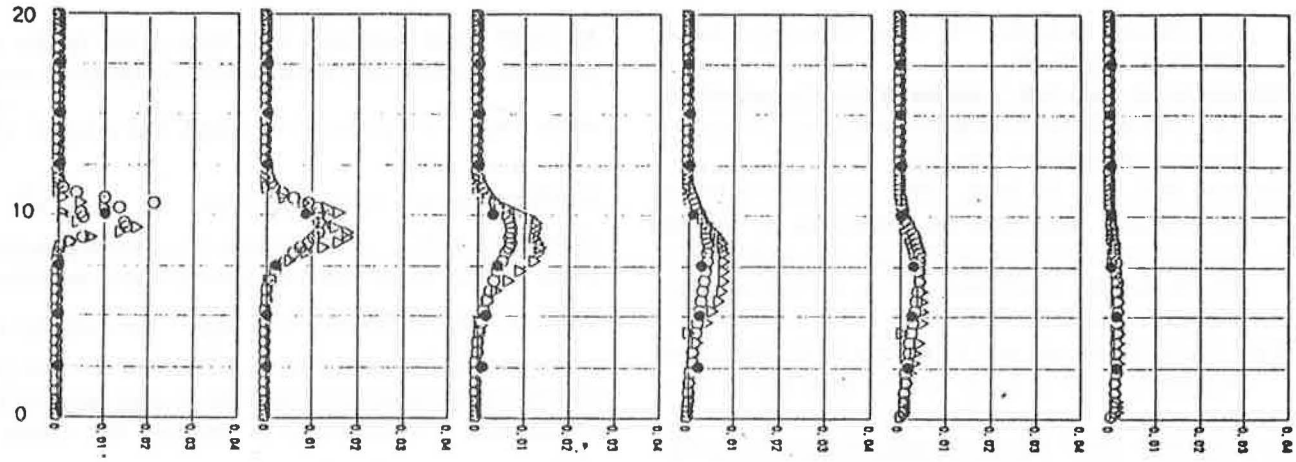

Figure A2 Distribution of $\overline{u_2^2}$.

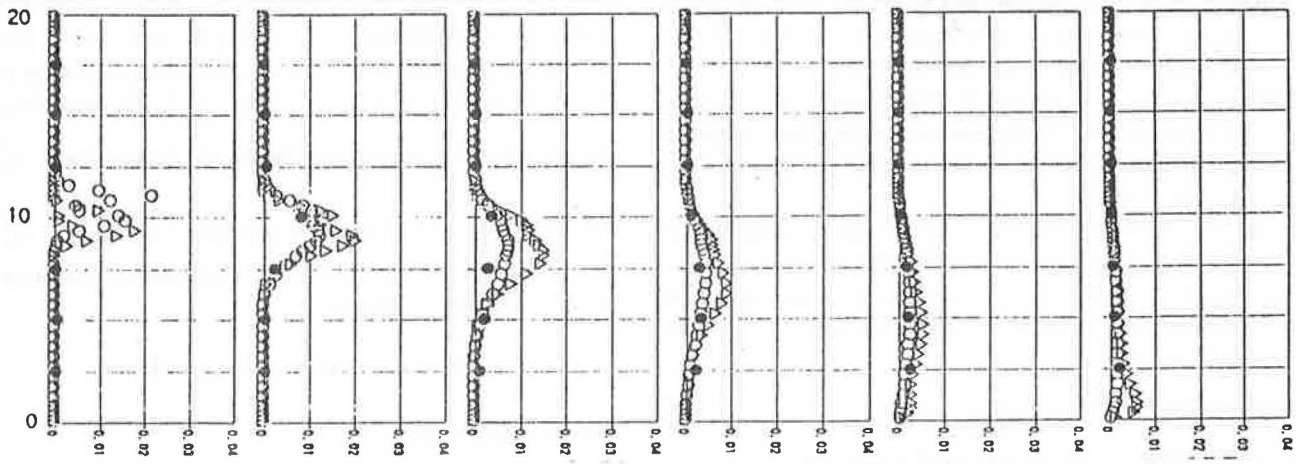

Figure A3 Distribution of $\overline{u_3^2}$.

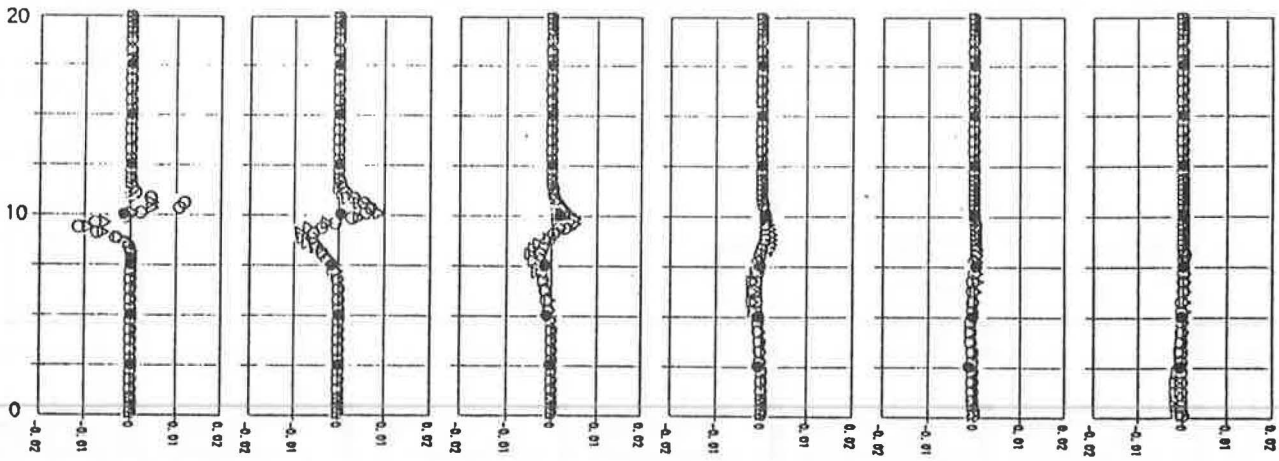

Figure A4 Distribution of $\overline{u_1 u_3}$.

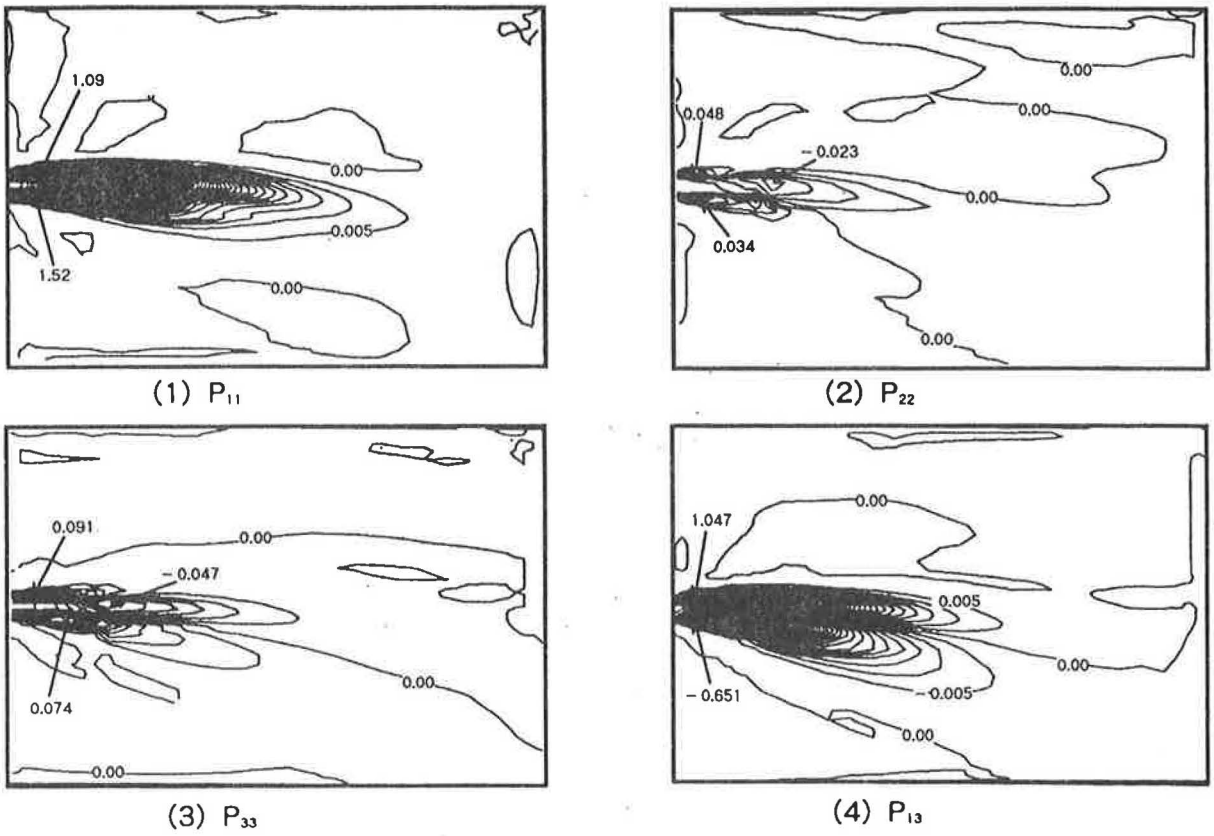

Figure A5 Distribution of P_{ij} *(generation term of* $\overline{u_i u_j}$ *by ASM at center section).*

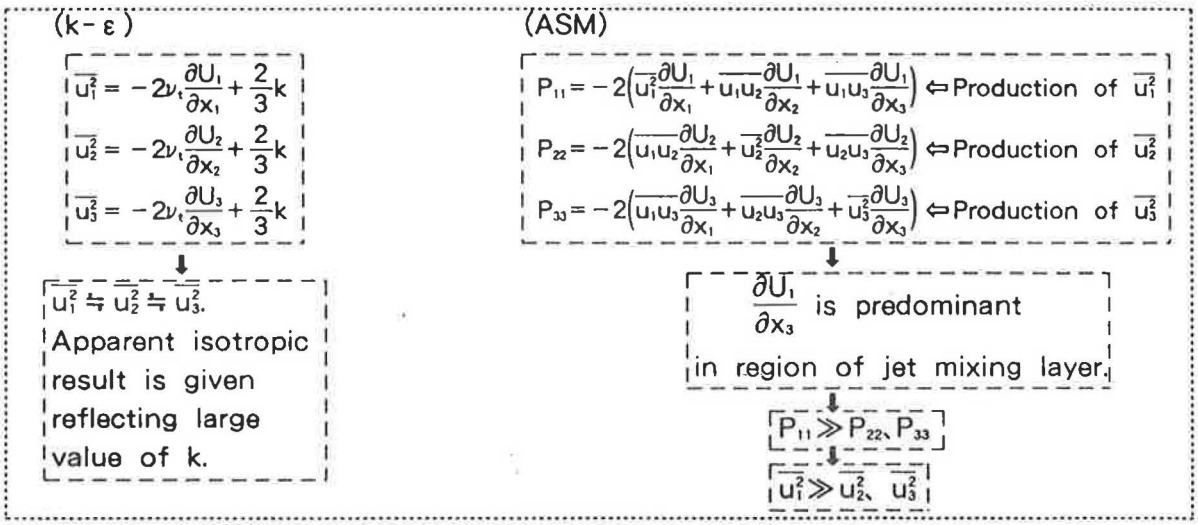

Figure A6 Difference of evaluation of $\overline{u_i u_j}$ *between* k-ε *model and ASM.*